Convergence and efficiency of global bases using proper orthogonal decomposition for capturing wind turbine wake aerodynamics

Juan Felipe Céspedes Moreno[1], Juan Pablo Murcia León[1], Søren Juhl Andersen[2]

[1]Department of Wind and Energy Systems, Technical University of Denmark, Frederiksborgvej 399, Roskilde, 4000, Denmark
[2]Department of Wind and Energy Systems, Technical University of Denmark, Anker Engelunds Vej 1, Kgs. Lyngby, 2800, Denmark

Correspondence to: Juan Felipe Céspedes (jfcm@dtu.dk)

Abstract. The Proper Orthogonal Decomposition (POD) can be applied by combining several datasets, i.e. using data obtained from simulations with different governing parameters. The resulting global POD basis is intended to represent all flows within the parameter space, and the convergence and efficiency of such global POD bases are evaluated here for the case of wind turbine wake aerodynamics in large wind farms. The analysis shows that the global POD bases have better performance across the parameter space than the optimal POD basis computed from a single dataset. The error associated with using a global basis across parameter space of reconstructions decreases and converges as more datasets are included, and there is a low sensitivity as to which datasets to include. It is also shown how this error is an order of magnitude smaller than the truncation error for 100 modes. Finally, the global basis applied to the highly turbulent flow within a wind farm has the advantage of providing consistent physical interpretability.

Keywords: Proper Orthogonal Decomposition, Global Basis, Reduced Order Modelling, Turbulence, Wind Turbine Wake Dynamics.

1 Introduction

The proper orthogonal decomposition (POD) is a classic data-driven method for decomposing fluctuations of turbulent flows into orthogonal modes, which provide an optimal linear decomposition in terms of the variance [Lumley (1967); Berkooz et al. (1993)]. POD has been applied on a vast range of different flow configurations, and the POD modes are typically used for one of two main applications. One, the modes can provide a physical interpretation of dominant coherent structures in complex turbulent flow, e.g. [Sirovich (1987), George (1988), Neumann and Wengle (2004), Meyer et al. (2007)]. Two, a truncated set of the modes can be used to construct reduced order models (ROMs), e.g. [Smith et al. (2005), Noack et al. (2011), Semaan et al. (2016), Taira et al. (2017)].

However, an optimal reconstruction in terms of variance might not always be the most desirable basis for creating ROMs. Alternative bases can for instance be derived by changing the norm to optimize other quantities instead of variance e.g. enthalpy, enstrophy, and dissipation [Colonius et al. (2002), Lee and Dowell (2020), Olesen et al. (2023)]. Emphasis can also be on the spectral content by performing POD in the frequency domain using Spectral POD [Sieber et al. (2016)] or the related

Dynamic Mode Decomposition [Schmid (2010)], which does not provide orthogonal bases. Furthermore, nonlinear bases can be formed using autoencoders, which constitute a nonlinear generalization of POD through an artificial neural network (ANN) [Hinton and Salakhutdinov (2006)]. Autoencoders are specifically designed to reduce the number of degrees of freedom required to describe a data set but might lack physical interpretability.

35 Irrespective of the decomposition method, the resulting bases are typically applied to data from a single flow. However, in cases of parametric studies, efforts have been made to transition between different bases to cover different flow cases [Christensen. et al. (1999), Stankiewicz et al. (2017), Xiao et al. (2017)]. Conversely, recent developments [Andersen and Murcia Leon (2022), Andersen and Murcia Leon (2023), Fu et al. (2023), Nony et al. (2022), Buoso et al. (2022)] employ a single global basis constructed by applying POD on a combination of multiple flow cases. The global basis maintains the

40 benefits of POD, namely orthogonality and physical interpretability. Using a global basis for constructing generic ROMs enables consistent physical analysis across different flow conditions using the same basis, and therefore holds the potential for constructing more robust POD models [Bergmann et al. (2009)] including diverse forms of interpolation across parameter space to predict unseen flow cases.

In a previous work, Andersen and Murcia Leon (2022) qualitatively compared the resulting global POD to POD modes derived

45 from individual flow cases. However, the efficiency of the global modes was not quantified. This article explores this aspect alongside the convergence of the global basis across the parameter space, which is expected in the POD formulation [Haasdonk (2013), Hesthaven et al. (2016)], and notions of how to select the datasets to create a global basis are also investigated in accordance to previous references [Haasdonk et al. (2011), Hesthaven et al. (2016), Quarteroni et al. (2016)]. The analysis uses a database of LES of wind turbine wake dynamics, which are particularly challenging as they are highly turbulent and

50 include the vast range of turbulent scales in the atmosphere. Therefore, this work contributes by explicitly showcasing the advantages and characteristics of global basis in ROMs applied in a practical and complex scenario.

2 Methodology

2.1 Flow Solver and Turbine Modelling

The LES database is the same as used for creating the predictive and stochastic reduced order model of wind turbine wakes

55 [Andersen and Murcia Leon (2022)], where the simulations were generated using the incompressible finite volume flow solver EllipSys3D [Michelsen (1992), Michelsen (1994), Sørensen (1995)]. A third-order QUICK scheme is used for the convective terms, and a second-order implicit method is used for time stepping. The pressure correction equation is solved with an improved version of the SIMPLEC algorithm [Shen et al. (2003)] and pressure decoupling is avoided using the Rhie-Chow interpolation technique. Large Eddie Simulations (LES) applies a spatial filter on the Navier–Stokes equations, where the

60 smaller scales are modeled through a sub-grid scale (SGS) model to achieve turbulence closure. The Deardorff SGS model is used [Deardorff (1980)].

The turbines are modeled using the actuator disc method, which imposes body forces in the flow equations [Mikkelsen (2004)]. Initially, the velocities are passed from EllipSys3D to Flex5 [Øye (1996)], which computes the forces and deflections through a full aero-servo-elastic computation, and transfers these back to EllipSys3D [Sørensen et al. (2015), Hodgson et al. (2021)].

2.2 Simulation Setup

The wind farm is simulated with 14 turbines aligned as shown in Fig.1. The computational domain is $192R \times 20R \times 20R$ in the streamwise, lateral, and vertical directions respectively. The grid is structured and has $3392 \times 192 \times 128 \approx 83 \times 10^6$ grid cells. The grid is equidistant from the inlet to the turbines and in the vicinity of the turbines, where it has a resolution of approximately 20 cells per blade radius. The grid is stretched towards the lateral, top, and outlet boundaries.

The turbines are separated by 12R in the streamwise direction, and 20R in the lateral direction. Cyclic boundary conditions are imposed on the lateral boundaries to mimic an infinitely wide wind farm. The modeled turbine is the NM80 turbine, which has a radius of R= 40.04m, hub-height of z_0= 80m, and rescaled rated wind speed of U_{rated}= 14m/s with a corresponding rated power of P_{rated}= 2.75MW [Aagaard Madsen et al. (2010)].
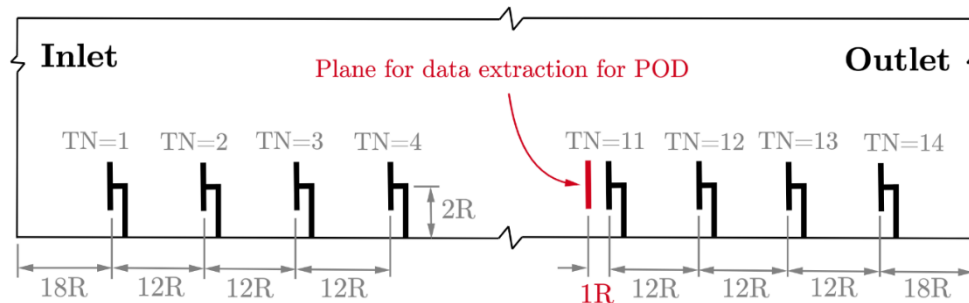
Figure 1: Simulation layout.

The neutral atmospheric boundary layer (ABL) inflow to the farm is modeled in a prior precursor simulation [Andersen and Murcia Leon (2022)]. The initial precursor simulation has a roughness of z_0= 0.05m and a friction velocity of u_*= 0.4545 m/s, which resulted in an average shear exponent of α = 0.14. The rough-wall boundary layer can be rescaled to model different wind speeds [Castro (2007)].

The flow database is limited to the incoming flow at each rotor, which captures the wake dynamics. Therefore, the three velocity components are extracted in vertical planes of $2R \times 2R$ located one radius upstream of each turbine to reduce the influence of turbine induction, see Fig. 1. This corresponds to a grid of 39×42 points in the y-z plane. The data is extracted every 0.1 seconds during 2×10^{17} time-steps, which is approximately 3.64 hours of simulated flow.

2.3 Parameter space and flow characteristics

The database is designed to cover the majority of the operational range for this particular wind farm, and therefore the parameter space governing the turbulent wake flow. The most important parameter for wind turbine wakes is the thrust coefficient C_T [van der Laan et al. (2020)]:

$$C_T = \frac{T}{\frac{1}{2}\rho A U^2} ,\tag{1}$$

Where T is the turbine's thrust, ρ is the air's density, A is the rotor's area, and U is the velocity. This coefficient is a relative measure of the force exerted by the turbine with respect to the momentum of the incoming wind. For low wind speeds, the turbine extracts as much energy as possible, and the thrust coefficient is typically around 0.8, which is considered high. Significantly higher values can result in flow reversal as the turbine enters propeller mode [Sørensen et al. (1998)]. For high wind speeds, the turbine typically pitches its blades to reduce power extraction and thrust force.

Four simulations were performed for different average incoming wind speeds, which cover a significant range of operating thrust coefficients. A second parameter inherently present in a wind farm is the turbine number (TN). As the flow enters the wind farm, the incoming wind for the first turbine is atmospheric, but the second turbine operates in the wake of the first turbine. Further inside the wind farm, multiple wakes can be present concurrently. Wakes have a significant impact on the performance of wind farms, as the wind speed is lower and the turbulent intensity is higher causing a reduction in power production and increased fatigue loads on turbines operating in the wake [Vermeer et al. (2003); Porté-Agel et al. (2020)].

The parameter space covered by the database is visualized in Fig. 2, which shows the time-averaged C_T of the wake-generating (i.e. upstream) turbine for the four different wind speeds (8 m/s, 12 m/s, 15 m/s, 20 m/s) as a function of the turbine number (2-14) for the turbines operating in the wake. C_T is approximately constant for all turbines at 0.8 and 0.3 for U = 8m/s and U = 20m/s, respectively. Effectively, the operation of the individual turbines does not change despite the presence of the wake, which in the latter case is minimal due to the low C_T. However, for U = 12-15 m/s there is a gradual transition in C_T from the first turbines to the turbines further into the farm, where the operating condition have converged as there is a balance between extracted power and wake recovery [Calaf et al. (2010)].The fully-developed or "infinite" wind farm is typically reached after the first 5-6 wind turbines [Andersen et al. (2020)].

Figure 2 shows 52 different combinations for the four wind speeds (U) and 13 turbine numbers (TN). Each combination corresponds to an inflow data set to a given turbine, $\mathbf{V}(y, z, t)$.
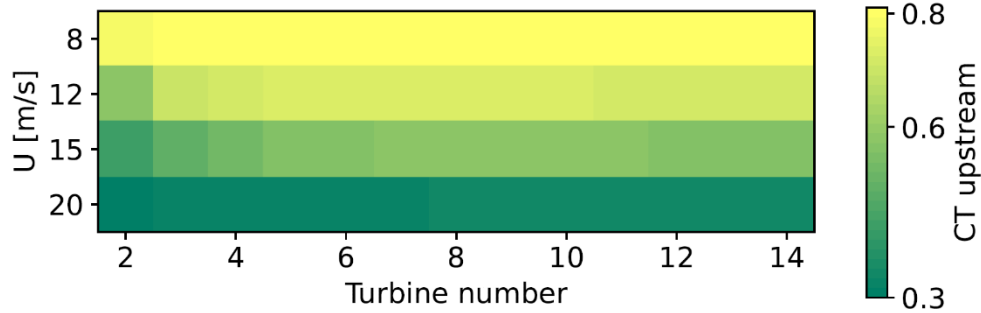
Figure 2: Parameter space from the Large Eddy Simulations. C_T is shown for the upstream turbine for each mean wind speed in the simulation inlet and turbine number.

2.4 Proper Orthogonal Decomposition

Proper Orthogonal Decomposition (POD) is a classic technique for dynamic flow analysis, which decomposes a turbulent flow into modes of spatial variability. These modes are orthogonal and, given the norm used to perform the decomposition, optimal in terms of capturing the variance of the fluctuating flow [Lumley (1967); Berkooz et al. (1993)].

The velocity field ($\mathbf{V}$) is described as the sum of the mean flow ($\bar{\mathbf{V}}$) and the fluctuating flow ($\mathbf{V}'$), as in Equation 2.

$$\mathbf{V}(y, z, t) = \bar{\mathbf{V}}(y, z) + \mathbf{V}'(y, z, t) \,, \tag{2}$$

POD is then applied to the three fluctuating velocity components of $\mathbf{V}'$ (u', v' and w'), where each time step is represented as a column vector, and N_t time steps are aggregated into a matrix $\mathbf{M} = [\mathbf{V}'_1, ..., \mathbf{V}'_{N_t}]$. The auto-covariance of $\mathbf{M}$ is computed: $\mathbf{R} = \mathbf{M}^T\mathbf{M}$, and the eigenvalue problem $\mathbf{RG} = \mathbf{G\Lambda}$ is solved, where $\mathbf{\Lambda}$ is a matrix of real and positive eigenvalues and $\mathbf{G}$ is a matrix of orthonormal eigenvectors $\mathbf{G} = [g_1, ..., g_{N_{t-1}}]$. The dimensionality has been reduced by 1 due to the extraction of the mean flow; and the orthonormality of the global modes is given using the standard inner product, $\langle \boldsymbol{a} ; \boldsymbol{b} \rangle = a_i b_i$, across all flow components: $\langle \boldsymbol{g_i} ; \boldsymbol{g_j} \rangle = \delta_{ij}$. Finally, the modes are organized according to the eigenvalue decay i.e., in descending order according to variance, representing the turbulent kinetic energy contribution of each mode. Collectively, all modes form a new set of basis functions spanning the data set.

The original flow can be reconstructed by projecting the flow into each mode with a standard inner product, which results in its contribution as a function of time (ϕ_i). Subsequently, as shown in equation 3, the modes multiplied by their contribution over time can be summed to reconstruct the flow.

$$\mathbf{V}'(y, z, t) \approx \sum_{i=0}^{K} g_i(y, z)\phi_i(t) \,, \tag{3}$$

An approximated reconstruction of the flow can be obtained by only including a limited number of modes ($K \leq N_{t-1}$).

2.5 Global POD basis

135 POD is traditionally applied on an individual flow case, i.e. on a "local" data set in the parameter space. Therefore, applying POD on a single data set is referred to as a *local POD basis* in the present work. The local basis contains the modes, which optimally represent the variance of that particular data set. Conversely, a *global POD basis* is formed by including multiple data sets in the decomposition [Andersen and Murcia Leon (2022)].

The global basis can be computed by including q different datasets, and adding N_T snapshots from each flow data set to the
140 matrix **M** before applying POD:

$$\mathbf{M} = \left[\mathbf{V}'_{1,1}, \dots, \mathbf{V}'_{1,N_t}, \dots, \mathbf{V}'_{q,1}, \dots, \mathbf{V}'_{q,N_t} \right], \tag{4}$$

Consequently, the global POD basis is sub-optimal at capturing the variance for a particular data set, but it is expected to provide a better representation across the entire parameter space.

2.6 Convergence of global POD basis

145 The expected sub-optimality of a global POD basis raises a number of central questions on the effectiveness relative to a local POD basis and on the required number and which datasets to include in the construction of a global POD basis.

Here, the parameter space contains 52 datasets. This means that for any number of datasets k composing a global base, there are $\binom{52}{k}$ possible global basis, so there are $\sum_{k=1}^{52} \binom{52}{k} = 4.5 \times 10^{15}$ possible combinations to generate a global basis, which effectively excludes the option of evaluating all of them. Consequently, the global POD bases are constructed in an iterative
150 manner, where the performance of a global basis is evaluated across all datasets in the parameter space. The dataset with the worst performance is added to the decomposition to gradually reduce the overall error and a new global POD basis is computed. The iterative procedure means that only 52 different combinations exist, as each data set can be chosen as the initial starting point.

3. Results

155 ### 3.1 Flow cases

The wake flows change considerably across the parameter space. Figure 3 shows the normalized average streamwise velocity and the turbulence intensity for the four corners of parameter space (Fig. 2).

(a) Mean wind speed in streamwise direction.	(b) Turbulence Intensity.
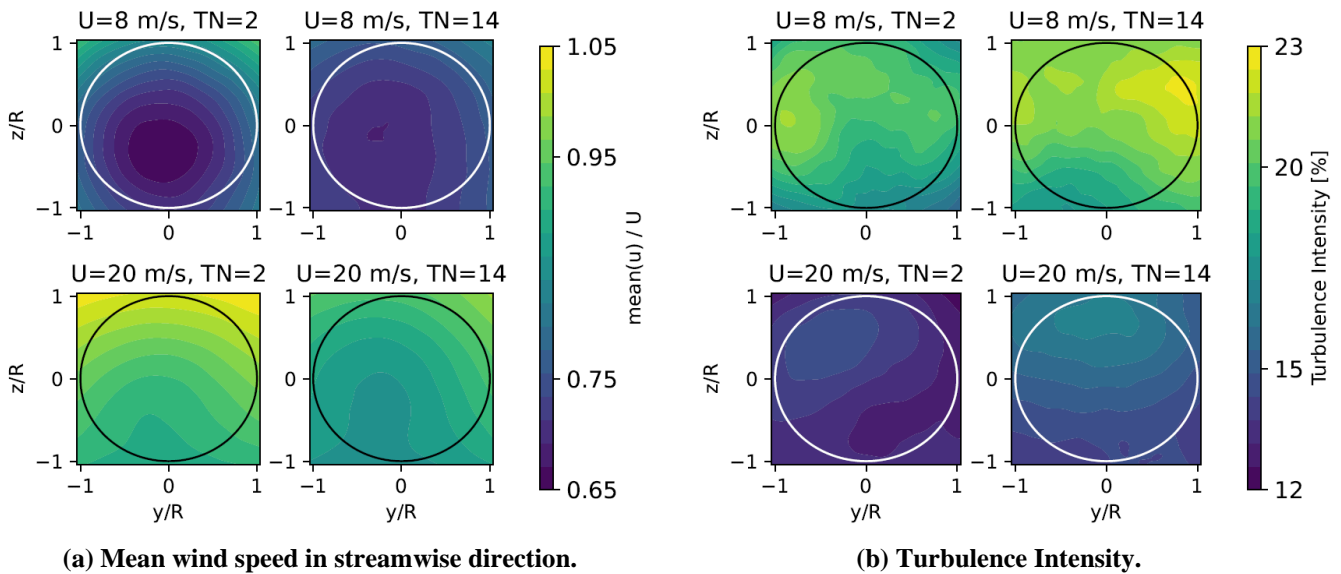
Figure 3: Mean streamwise wind speed and turbulence intensity of the flows in the four corners of the parameter space. The circle on each plot represents the rotor.

Figure 3a shows a significantly larger deficit and a more circular wake when C_T is high (U=8 m/s), and a less significant wake and more dominant shear profile from the atmospheric boundary layer when C_T is low (U=20~m/s). Furthermore, the spatial gradients are less pronounced late in the wind farm (TN=14), which is a consequence of the increased mixing due to the presence of multiple wakes. Figure 3b shows the streamwise turbulence intensity ($\sigma(u')/U$), which ranges from 12% up to 23% with the largest values in flows with a high thrust coefficient. The highest turbulence intensity is located in the upper half of the domain, where more momentum is exchanged between the wake and the surrounding atmospheric flow.

Figure 4 shows the streamwise velocity spectra taken at the rotor center for the four corners of the parameter space. This exemplifies how turbulent dynamics depend on both the thrust coefficient and turbine number. The total turbulent kinetic energy is larger for the high wind speed, as expected. The spectrums tend to shift at the low frequencies, particularly for high C_T, as the largest turbulent length scales are broken down as they move through the wind farm [Andersen et al. (2017)].
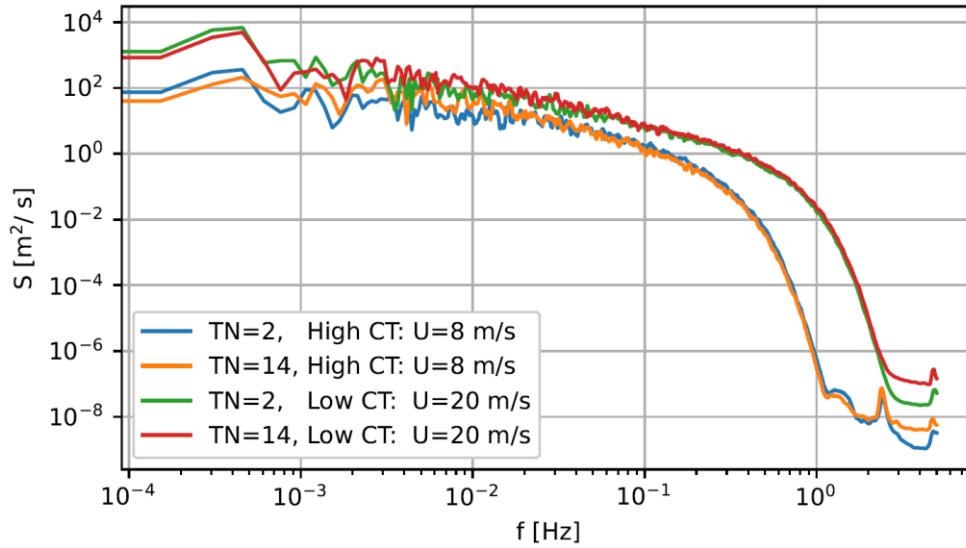
Figure 4: Fourier spectra of u′ at hub height for the four corners of the parameter space.

3.2 Global modes

POD is applied to compute the local and global POD bases. Figure 5 shows the first eight local modes calculated with one dataset from the parameter space, 1P. The figure also shows eight global POD modes derived using 9 datasets, 9P. The local and global modes are clearly similar, and there is a general trend that the turbulent structures diminish in size for higher modes. However, these are not the first eight global POD modes, but rather the eight modes most qualitatively comparable to the first eight local POD modes. This is an important point of the global basis. The ordering of the individual modes might change. For instance, global mode 9P g_7 is not shown as it qualitatively corresponds to local mode 1P g_9, while global modes 9P g_7 and 9P g_8 are more important over the parameter space. As shown by Andersen and Murcia Leon (2023), this means that the contribution of variance captured by each mode might change over the parameter space. The analysis is kept qualitative here, but a more quantitative comparison of the re-ordering and similarity of modes from different bases has been proposed by Olesen et al. (2024).
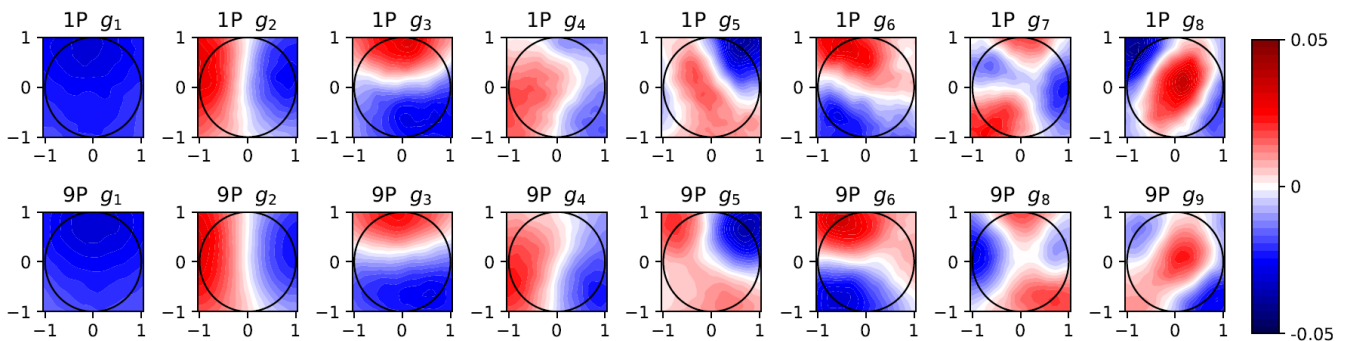
Figure 5: Streamwise component of the first modes using one and nine points from parameter space, 1P and 9P respectively. The circle on each mode represents the turbine rotor.

3.3 Global modes convergence

Although qualitatively comparable, the global basis must be both efficient and representative of the entire parameter space. A basis is evaluated against the full LES flow using a velocity error E_{vel} defined in equations 5 and 6. The metric takes, for every velocity component, the average in space (y,z) of the ratio between the root mean square error of the velocity field and its standard deviation over time. The error is normalized by the standard deviation because it is a direct measure of the variance in the original flow. Subsequently, E_{vel} corresponds to the norm of the errors from the three velocity components. This results in a single value for each point in the parameter space representing the total error of the reconstruction with respect to the original flow.

The velocity error is shown in Figure 6a, where the top left figure corresponds to the local basis using one dataset of U = 8m/s and TN = 14, indicated by the white number. This basis is evaluated across the entire parameter space using 100 modes, i.e. the basis derived from the one dataset is applied on all flows. It reveals that the velocity error is largest at the first turbines for U = 8m/s. However, the velocity error is low for the high wind speed, which indicates an efficient reconstruction of very different flows.

$$E_{u\prime} = \text{mean}_{y,z} \left[\frac{\sqrt{\text{mean}_t [u'_{\text{LES}}(y,z,t) - u'_{\text{POD}}(y,z,t)]^2}}{\text{std}_t [u'_{\text{LES}}(y,z,t)]} \right], \tag{5}$$

$$E_{\text{vel}} = \sqrt{E_{u\prime}^2 + E_{v\prime}^2 + E_{w\prime}^2}, \tag{6}$$
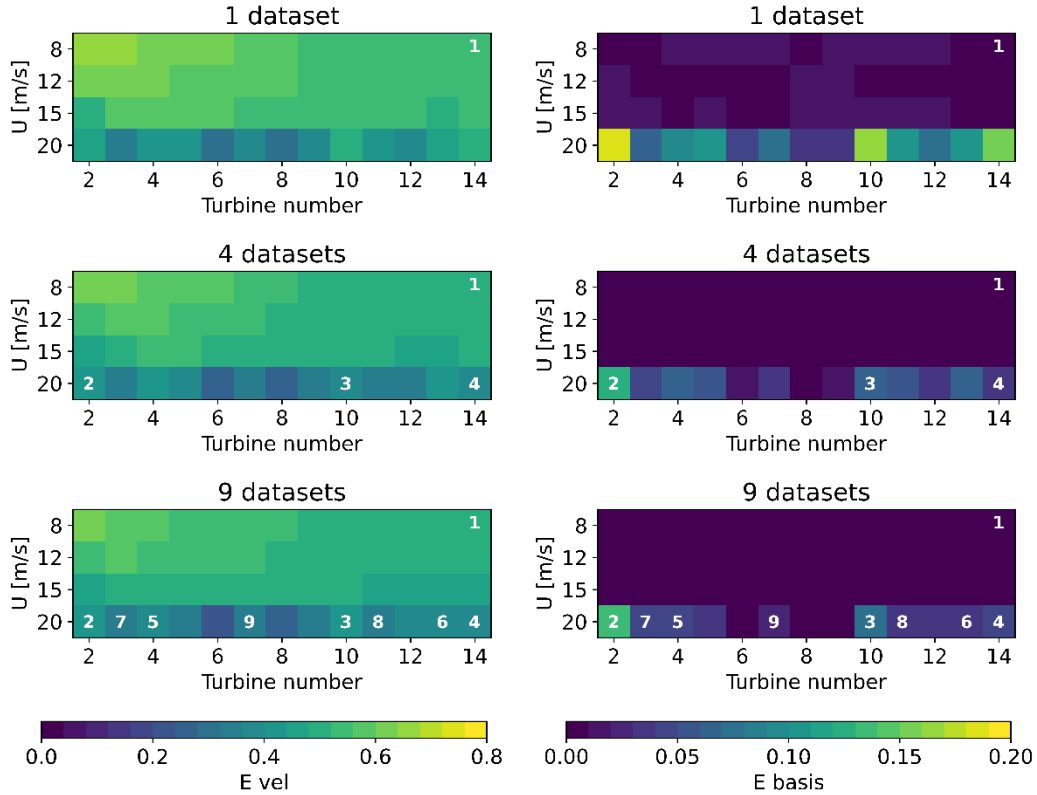
(a) **Velocity error fields in parameter space**   (b) **Basis error fields in parameter space**

Figure 6: Velocity error (E_{vel}) and basis error (E_{basis}) using 100 modes across the parameter space for basis including 1, 4, and 9 datasets.

The velocity error (E_{vel}) corresponds to the total error with respect to LES, but this has two components: a truncation error due to the number of modes included, and a basis error E_{basis} due to the use of a global basis, which is non-optimal basis locally. The basis error arises because a better basis is capable of reconstructing a larger portion of the flow with the same number of modes. Therefore, in order to isolate and quantify the basis error, the velocity error from the local POD bases ($E_{vel-local\,POD}$) is subtracted from E_{vel}, as shown in equation 7.

$$E_{basis} = E_{vel} - E_{vel-local\,POD} \,, \tag{7}$$

The basis error is shown in Fig. 6b. Contrarily to the velocity error E_{vel}, the largest basis errors correspond to the low C_T. Hence, the dataset for $U = 20$ m/s and $TN = 2$ with the largest basis error is added to improve the global basis. The same error estimates are computed with the updated global basis, and the procedure is iterated to reduce the overall error of the global basis.

220   Figure 6 shows the evolution of errors using four and nine datasets. The white numbers indicate the order of adding the different

datasets to the global basis. The average errors are clearly reduced when more datasets are included. Additionally, the largest

basis errors remain at low C_T, and the difference of including one or four datasets is significantly larger than using four or nine

datasets, which suggests convergence of the global basis.

Figure 6 uses U=8 m/s and TN=14 as initial dataset for the iterative procedure. Table 1 shows five different starting points.

225   The first four initial datasets correspond to the four corners of parameter space, and the fifth is a point in the middle of the

domain.

Coordinates	Name				
	A	**B**	**C**	**D**	**E**
U [m/s]	8	20	8	20	15
TN	2	2	14	14	5

Table 1: Initial datasets from parameter space.

Figure 7 shows the evolution of the average velocity error (E_{vel}) across parameter space as a function of the number of datasets

230   in the global basis for the five different initial conditions. As seen, all five initial conditions (A-E) yield the same trend of

decreasing the mean velocity error as more datasets are included. On average the mean velocity error decreases 6% from one

to nine datasets. It is noted how the influence of the starting point decreases as more datasets are included. For instance, with

one dataset, the relative difference between the best and worst performing global basis is 3.9%, but with nine datasets it is

reduced to 0.4%. Furthermore, after including three datasets, the iterations starting at points B and D (those which started at

235   U= 20 m/s) contain the same datasets, which means that from that point they yield the same results.

The examined bases A-E include 512 snapshots per dataset and the flow reconstruction was truncated at 100 modes. The

horizontal lines in Fig. 7 indicate the average error when each flow in the parameter space is reconstructed with 100 modes of

the corresponding local basis, computed using 512, 1024, and 2048 snapshots respectively. The performance of these bases

depends on the number of snapshots before achieving convergence, and the number of independent snapshots is limited, at

240   around 2048, by the span of a single dataset. On the other hand, a global basis can include more data because it is extracted

from different datasets, i.e. different flows, which makes the snapshots independent.
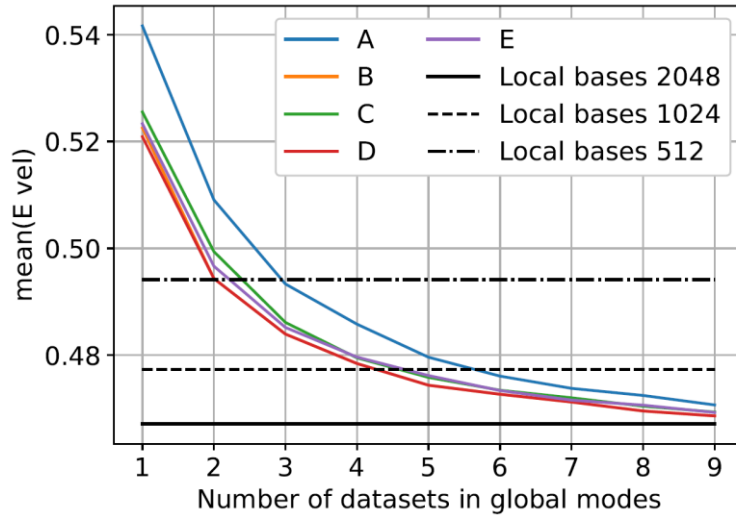
Figure 7: Mean error E_{vel} across the parameter space using 100 modes vs the number of datasets included in the global basis.

245

Consequently, global bases can be directly compared to local bases when computed with the same amount of data. Table 2 compares the values of the horizontal lines in Fig. 7 (local bases error) with the average result from the curves A-E at the corresponding number of snapshots. As more datasets are included, the performance of the global bases gets closer to the theoretical minimum error of the local bases, where four datasets correspond to a relative difference in the error of 2.8%

250   truncated at 100 modes.

Total number of snapshots	Local bases error	Global bases		Relative error difference
		Number of datasets	Average error	
512	0.494	1	0.527	6.7%
1024	0.477	2	0.499	4.6%
2048	0.467	4	0.480	2.8%

Table 2: Mean velocity error comparison between local bases and global bases (average of curves A-E) with the same total number of snapshots using 100 modes.

255   For the dependence of the number of truncation modes, Fig. 8 shows the velocity error for two local and three global bases truncating at different numbers of modes. Overall, the error decreases as more modes are included. Here, it is also possible to compare the truncation error to the basis error. The basis error is approximately one order of magnitude smaller than the truncation error. For instance, using 100 modes, the error of the global basis using 1 dataset is 0.523, and the error of the best bases, i.e. local bases 2048, is 0.469, which is a relative difference of approximately 10%.
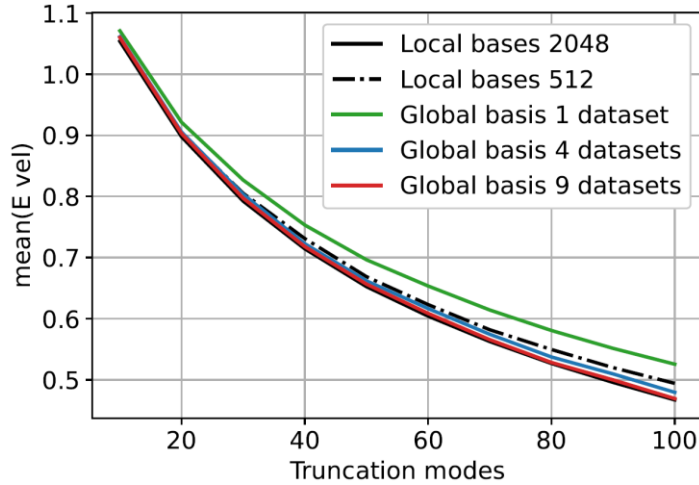
Figure 8: Mean error E$_{vel}$ across the parameter space vs number of truncation modes. The global bases shown correspond to the starting point C from table 1.

It is noteworthy, especially for a global basis with a low number of datasets, that the basis error increases as more modes are included for the number of modes plotted. This is attributed to the fact that each additional mode from the optimal basis adds more information to the flow than a mode from the sub-optimal base. However, any of these bases are capable of completely reconstructing the flow if all modes are included. Therefore, it is expected that as more modes are included, the optimal bases start to saturate, while the sub-optimal bases eventually will catch up and the basis error gap will reduce.

3.4 Case study with stochasticity

The physical and statistical implications of employing a global basis are investigated by applying it to the LES case of U = 12m/s, where the turbines have an average C$_T$= 0.71. The chosen global basis is generated based on four datasets shown in Fig. 6, which yield a basis error of 2.8%, see Table 2. Furthermore, the employed global basis does not contain information from this flow scenario.

The analysis focuses on spectral statistics by utilizing the stochastic engine of PS-ROM Andersen and Murcia Leon (2022), but does not include the predictive part, i.e. the actual projected spectrums are used, similar to Andersen and Murcia Leon (2023). In all cases, the spectrum analyzed is of the streamwise velocity at the rotor's center. Two different spectra will be compared using the spectral error metric shown in equation 8:

$$E_{S-i,j} \equiv \frac{\int (\hat{s}_i - \hat{s}_j)df}{\int \hat{s}_j \, df} \,, \tag{8}$$

where E_S stands for error in the spectra, S_i and S_j are the two spectra to compare. $\hat{S}_i$ is S_i filtered with a rolling mean using an averaging window varying logarithmically in size to smooth out higher frequencies.

The inherent stochastic variability is assessed by generating N=30 stochastic realizations and cross-comparing all realizations against themselves for a single flow case. This yields a total of $\binom{N}{2} = 435$ spectral error samples. The distributions of stochastic errors are shown in Fig. 9. The red distributions are all centered around zero as the spectral error here measures the stochastic variability of the 30 realizations relative to themselves, i.e. how much can a single realization of a constructed flow
285   scenario vary relative to numerous realizations of the same flow. The distributions tend to narrow further into the wind farm, which indicates how the deep farm flows become increasingly self-organized and governed by the wakes Andersen et al. (2017).

This development can also be examined by comparing the spectral error between different flows, i.e. comparing 30 stochastic flow realizations at each turbine against the inflow to a specific turbine. Here, the last turbine (TN=14) is chosen to represent
290   the fully-developed wind farm. The spectral error given by equation 8 is also used for this comparison, which yields $N^2 = 900$ error samples if both flow cases have N=30 stochastic realizations. The corresponding errors are shown as green distributions in Fig. 9. The distributions for the first turbines are significantly offset with a negative error, but initially narrower than the stochastic distributions. Eventually, the green distributions gradually become centered around zero. Hence, the distributions of the stochastic spectral error and the spectral error relative to the 14th turbine can be compared directly to
295   determine if there is a statistical difference between inflow to a given turbine relative to the last turbine. If the error distributions are reflections of each other, it implies that there is no statistical difference between the velocity spectra at the center of the domain between the turbine number in question and turbine number 14. This is particularly useful when trying to determine if the flow dynamics have reached the fully-developed wind farm conditions, where the statistical distributions no longer change as the turbine number increases Andersen et al. (2015). This is the case from approximately TN=9 forwards.
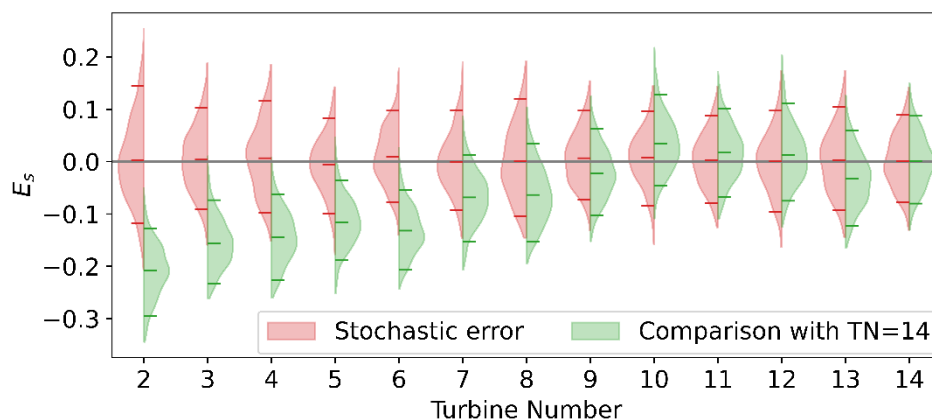
300

Figure 9: Distributions of spectral errors for the streamwise velocity at the rotor's center related to the stochasticity and relative to turbine number 14 through the wind farm using 30 stochastic realizations and 100 global POD modes for the simulation case U=12 m/s.

305   The results from Fig. 9 are based on the comparison of streamwise velocity spectra at the rotor's center, but the contribution of individual modes to the different flow cases can also be compared. Figure 10 shows similar spectral error distributions for global modes 2, 5, 12, and 20. Modes 2 and 5 show a gradual evolution reminiscing of Fig. 9, where the distributions gradually become increasingly similar. Contrarily, higher modes, such as 12 and 20, present a more scattered behavior with lower errors and mean values varying between positive and negative for TN > 2. This suggests that the transition to a deep wind farm state

310   is primarily dictated by changes in the first global modes, which are associated with the largest turbulent scales. This trend corroborates the findings of Andersen and Murcia Leon (2023), where it was clearly shown how different global modes are actuated for different locations in the wind farm.
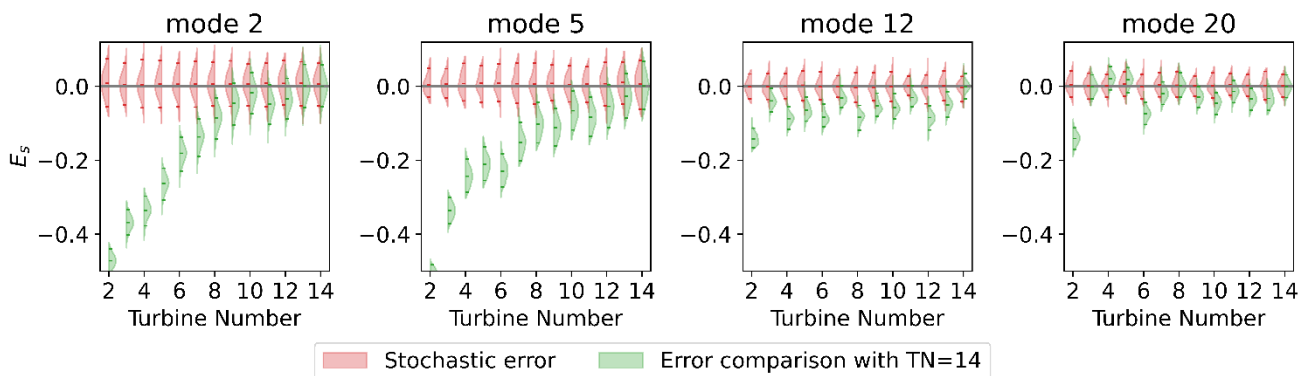
Figure 10: Distributions of spectral errors for four modes related to the stochasticity and relative to turbine number

315   **14 through the wind farm using 30 stochastic realizations for the simulation case U= 12m/s.**

4 Discussion

Employing a global POD basis allows the use of the same modes for an entire parameter space but introduces the basis error in the flow reconstructions (equation 7). The basis error emerges because the global basis is not as efficient at reconstructing

320   a particular flow as the local POD basis. However, it was shown that this error is reduced as more datasets are included on the global basis, and it is approximately one order of magnitude smaller than the truncation error for 100 modes.

The convergence of the global POD basis as a function of the number of datasets has a parallel with the convergence of the local POD basis. A local POD basis converges when enough snapshots of the flow are included, so it contains information about all the dynamics that occur in the flow [Hekmati et al. (2011)]. Consequently, it is an optimal basis in terms of variance,

325   and including more snapshots would not improve its performance. Similarly, for the global POD basis, as more datasets are added, more information on the dynamics of the flows across parameter space is included. On the limit, when sufficient information covering the parameter space has been supplied, including additional datasets with flow dynamics that have already been covered will not improve the performance of the basis.

The inclusion of more datasets in the global modes implied adding more data in total, as the number of snapshots per dataset
330 was kept constant. A different approach is to keep the amount of snapshots constant, and hence include fewer snapshots per
dataset; which would reduce the time to compute the modes that scales quadratically with the number of snapshots. This is an
unexplored scenario, but it is speculated that it would only be useful as long as there are enough snapshots per dataset to
generate an acceptable local POD basis with them, which would imply that there is enough information per dataset to capture
its dynamics.

335 The systematic process of including addition datasets is focussed on minimizing the basis error (equation 7) with respect to
the local bases' performance. The iterative procedure particularly identifies adding more datasets with low C_T. However,
additional datasets could be identified using alternative metric, e.g. the velocity error, which would prioritize adding datasets
of low turbine numbers and high C_T. Applying such alternative metrics, or even including arbitrary datasets scattered in the
parameter space, also results in a reduction of the error as the number of datasets increases.

340 Furthermore, it might be impractical to perform a detailed and systematic convergence study of the global basis for all
applications. However, the present analysis also shows how the global basis is relatively insensitive to which datasets are used.
It is therefore generally recommended to use datasets, which represent various key flow phenomena. Nevertheless, selecting
key datasets apriori would typically require domain knowledge to identify key scenarios to model.

Here, the global bases are used to model and analyze highly turbulent wind turbine wakes, but the use of global bases is
345 expected to be generally applicable. The present work expands the parameter space to cover two dimensions compared to the
single parameter in Andersen and Murcia Leon (2022), and there are no principal limits to the number of dimensions. However,
it is speculated that if the same set of modes is used in an extremely large parameter space, their efficiency becomes
considerably lower than the local POD modes at a given point in parameter space, and more modes would be required for the
flow generation.

350 Finally, the case study highlights a number of benefits of employing a global basis. The global basis enables detailed and
quantifiable physical interpretation of how the flow changes within the parameter space, as also seen in Andersen and Murcia
Leon (2023), where the modal statistics of a global POD basis applied on a full wind farm clearly reveal three main flow
regimes of atmospheric inflow, single wake and multiple wakes. The expansion of the parameter space reveals new insights
compared to Andersen and Murcia Leon (2022). For instance, it is clearly seen how the spectral error distributions converge
355 further into the wind farm indicating when fully-developed wind farm flow conditions are achieved dynamically and how this
is linked to the first few modes. The method also enables modelers to estimate both the impact and uncertainty of different
realizations as well as different modes when generating synthetic turbulent flows. Additionally, the analysis also reveals how
wind turbine wakes are relatively coherent flows, which can be covered by approximately 100 modes. Although, the
consistently larger basis error for U= 20m/s also highlights how more modes are required to reduce the errors for more
360 atmospheric flows, where the influence of the turbines is negligible.

5. Conclusions

Global POD bases are shown to provide an efficient basis to represent an entire parameter space. This allows direct comparisons of the role of each mode in different flows, which facilitates dynamic analysis of the different flow cases throughout the parameter space.

The performance of the global basis has an error with respect to the local POD basis. But it is one order of magnitude lower than the truncation error. And most importantly, it is significantly reduced and exhibits convergence towards the local POD basis as more datasets are included in the global basis.

The selection of datasets to include is not necessarily crucial for producing an efficient global basis, especially when the basis error is compared to the truncation error of the flow reconstruction or the stochastic variability of flow realizations. However, including key features from the different flows across the parameter space is recommended.

6. Acknowledgements

Computational resources have been provided by the DTU cluster Sophia. DTU Computing Center Technical University of Denmark (2022) and the work has been partly funded by DTU Wind Energy through the Wind Farm Flow CCA 2022.

7. Competing interests

The authors declare that they have no known competing financial interests or personal relationships that could have appeared to influence the work reported in this paper.

8. Author contribution

The three authors conceived the idea of this article based on previous work developed by Andersen and Murcia Leon. The LES simulations were done by Andersen, and Cespedes did the POD calculations and convergence of the global modes based on a code previously developed mainly by Murcia Leon. Finally, the writing and revision of this article was equally distributed among the three authors.

References

Aagaard Madsen, H., Bak, C., Schmidt Paulsen, U., Gaunaa, M., Fuglsang, P., Romblad, J., Olesen, N., Enevoldsen, P., Laursen, J., Jensen, L., 2010. The DAN-AERO MW Experiments: Final report. Number 1726(EN) in Denmark. Forskningscenter Risoe. Risoe-R, Danmarks Tekniske Universitet, Risø Nationallaboratoriet for Bæredygtig Energi.

Andersen, S., Witha, B., Breton, S.P., Sørensen, J., Mikkelsen, R., Ivanell, S., 2015. Quantifying variability of large eddy simulations of very large wind farms. Journal of Physics: Conference Series (Online) 625. doi:10.1088/1742-6596/625/1/012027.

390 Andersen, S.J., Breton, S.P., Witha, B., Ivanell, S., Sørensen, J.N., 2020. Global trends of large wind farm performance based on high fidelity simulations. Wind Energy Science Discussions 2020, 1–27. doi:10.5194/wes-2019-109.

Andersen, S.J., Murcia Leon, J.P., 2022. Predictive and stochastic reducedorder modeling of wind turbine wake dynamics. Wind Energy Science 7, 2117–2133. doi:10.5194/wes-7-2117-2022.

Andersen, S.J., Murcia Leon, J.P., 2023. Stochastic wind farm flow generation using a reduced order model of les. Journal of

395 Physics: Conference Series 2505, 012050. doi:10.1088/1742-6596/2505/1/012050.

Andersen, S.J., Sørensen, J.N., Mikkelsen, R.F., 2017. Turbulence and entrainment length scales in large wind farms. Philosophical Transactions of the Royal Society of London A: Mathematical, Physical and Engineering Sciences 375. doi:10.1098/rsta.2016.0107.

Bergmann, M., Bruneau, C.H., Iollo, A., 2009. Enablers for robust pod models. Journal of Computational Physics 228, 516–

400 538. URL:https://www.sciencedirect.com/science/article/pii/S002199910800510X, doi:https://doi.org/10.1016/j.jcp.2008.09.024

Berkooz, G., Holmes, P., Lumley, J.L., 1993. The proper orthogonal decomposition in the analysis of turbulent flows. Annual Review of Fluid Mechanics 25, 539–575. doi:10.1146/annurev.fl.25.010193.002543.

Buoso, S., Manzoni, A., Alkadhi, H., Kurtcuoglu, V., 2022. Stabilized reduced-order models for unsteady incompressible

405 flows in threedimensional parametrized domains. Computers & Fluids 246, 105604. doi:10.1016/j.compfluid.2022.105604.

Calaf, M., Meneveau, C., Meyers, J., 2010. Large eddy simulation study of fully developed wind-turbine array boundary layers. Physics of fluids 22, 015110. doi:10.1063/1.3291077.

Castro, I.P., 2007. Rough-wall boundary layers: mean flow universality. Journal of Fluid Mechanics 585, 469–485. doi:10.1017/S0022112007006921.

410 Christensen., E.A., Brøns, M., Sørensen, J.N., 1999. Evaluation of proper orthogonal decomposition–based decomposition techniques applied to parameter-dependent nonturbulent flows. SIAM Journal on Scientific Computing 21, 1419–1434. doi:10.1137/S1064827598333181.

Colonius, T., Rowley, C., Freund, J., Murray, R., 2002. On the choice of norm for modeling compressible flow dynamics at reduced-order using the pod, in: Proceedings of the 41st IEEE Conference on Decision and Control, 2002., pp. 3273–3278

415 vol.3. doi:10.1109/CDC.2002.1184376.

Deardorff, J.W., 1980. Stratocumulus-capped mixed layers derived from a three-dimensional model. Boundary-Layer Meteorology 18, 495–527. doi:10.1007/BF00119502.

Fu, J., Xiao, D., Fu, R., Li, C., Zhu, C., Arcucci, R., Navon, I.M., 2023. Physics-data combined machine learning for parametric reducedorder modelling of nonlinear dynamical systems in small-data regimes. Computer Methods in Applied Mechanics and

420 Engineering 404, 115771. doi:10.1016/j.cma.2022.115771.

George, W.K., 1988. Insight into the dynamics of coherent structures from a proper orthogonal decomposition. Proceedings of the International Centre for Heat and Mass Transfer , 469–487.

Haasdonk, B., 2013. Convergence rates of the pod–greedy method. ESAIM: Mathematical Modelling and Numerical Analysis 47, 859–873. doi:10.1051/m2an/2012045.

Haasdonk, B., Dihlmann, M., Ohlberger, M., 2011. A training set and multiple bases generation approach for parameterized model reduction based on adaptive grids in parameter space. Mathematical and Computer Modelling of Dynamical Systems 17, 423–442. doi:10.1080/13873954.2011.547674.

Hekmati, A., Ricot, D., Druault, P., 2011. About the convergence of POD and EPOD modes computed from CFD simulation. Computers & Fluids 50, 60–71. doi:https://doi.org/10.1016/j.compfluid.2011.06.018.

Hesthaven, J.S., Rozza, G., Stamm, B., 2016. Certified Reduced Basis Meth ods for Parametrized Partial Differential Equations. Springer International Publishing. doi:10.1007/978-3-319-22470-1.

Hinton, G.E., Salakhutdinov, R.R., 2006. Reducing the dimensionality of data with neural networks. Science 313, 504–507. doi:10.1126/science.1127647.

Hodgson, E.L., Andersen, S.J., Troldborg, N., Forsting, A.M., Mikkelsen, R.F., Sørensen, J.N., 2021. A quantitative comparison of aeroelastic computations using flex5 and actuator methods in les. Journal of Physics: Conference Series 1934, 012014. doi:10.1088/1742-6596/1934/1/012014.

van der Laan, M., Andersen, S., Kelly, M., Baungaard, M., 2020. Fluid scaling laws of idealized wind farm simulations. Journal of Physics: Conference Series 1618, 062018. doi:10.1088/1742-6596/1618/6/062018.

Lee, M.W., Dowell, E.H., 2020. Improving the predictable accuracy of fluid Galerkin reduced-order models using two POD bases. Nonlinear Dynamics 101, 1457–1471. doi:10.1007/s11071-020-05833-x.

Lumley, J.L., 1967. The structure of inhomogeneous turbulence. Atmospheric turbulence and wave propagation , 166–178.

Meyer, K.E., Pedersen, J.M., Özcan, O., 2007. A turbulent jet in crossflow analysed with proper orthogonal decomposition. Journal of Fluid Mechanics 583, 199–227. doi:10.1017/S0022112007006143.

Michelsen, J.A., 1992. Basis3D - a Platform for Development of Multiblock PDE Solvers: - release. volume AFM 92-05. Technical University of Denmark.

Michelsen, J.A., 1994. Block structured Multigrid solution of 2D and 3D elliptic PDE's. Technical Report Technical University of Denmark AFM 94-06.

Mikkelsen, R.F., 2004. Actuator Disc Methods Applied to Wind Turbines. Ph.D. thesis. Technical University of Denmark.

Neumann, J., Wengle, H., 2004. Coherent structures in controlled separated flow over sharp-edged and rounded steps. Journal of Turbulence 5, N22. doi:10.1088/1468-5248/5/1/022.

Noack, B., Morzyanski, M., Tadmor, G., 2011. Reduced-Order Modelling for Flow Control. Courses and lectures, SpringerWienNewYork.

Nony, B.X., Rochoux, M., Jaravel, T., Lucor, D., 2022. Reduced-order modelling for parameterized large-eddy simulations of atmospheric pollutant dispersion. arXiv:2208.01518.

455 Olesen, P.J., Hodzic, A., Andersen, S.J., Sørensen, N.N., Velte, C.M., 2023. Dissipation-optimized proper orthogonal decomposition. Physics of Fluids 35, 015131. doi:10.1063/5.0131923.

Olesen, P.J., Soucasse, L., Podvin, B., Velte, C.M., 2024. Dissipation-based proper orthogonal decomposition of turbulent Rayleigh–Bénard convection flow. Physics of Fluids 36, 035109. doi:10.1063/5.0188430.

Øye, S., 1996. Flex4 simulation of wind turbine dynamics. 28th IEA Meeting of Experts Concerning State of the Art of
460 Aeroelastic Codes for Wind Turbine Calculations , 71–76.

Porté-Agel, F., Bastankhah, M., Shamsoddin, S., 2020. Wind-turbine and wind-farm flows: A review. Boundary-Layer Meteorology 174, 1–59. doi:10.1007/s10546-019-00473-0.

Quarteroni, A., Manzoni, A., Negri, F., 2016. RB Methods: Basic Principles, Basic Properties. doi:10.1007/978-3-319-15431-2_3.

465 Schmid, P.J., 2010. Dynamic mode decomposition of numerical and experimental data. Journal of Fluid Mechanics 656, 5–28. doi:10.1017/S0022112010001217.

Semaan, R., Kumar, P., Burnazzi, M., Tissot, G., Cordier, L., Noack, B.R., 2016. Reduced-order modelling of the flow around a high-lift configuration with unsteady coanda blowing. Journal of Fluid Mechanics 800, 72–110. doi:10.1017/jfm.2016.380.

Shen, W.Z., Michelsen, J.A., Sørensen, N.N., Sørensen, J.N., 2003. An improved simplec method on collocated grids for
470 steady and unsteady flow computations. Numerical Heat Transfer, Part B: Fundamentals 43, 221–239. doi:10.1080/713836202.

Sieber, M., Paschereit, C.O., Oberleithner, K., 2016. Spectral proper orthogonal decomposition. Journal of Fluid Mechanics 792, 798–828. doi:10.1017/jfm.2016.103.

Sirovich, L., 1987. Turbulence and the dynamics of coherent structures. I. coherent structures. Quarterly of Applied
475 Mathematics 45, 561–70. doi:10.1090/qam/910462.

Smith, T.R., Moehlis, J., Holmes, P., 2005. Low-dimensional models for turbulent plane couette flow in a minimal flow unit. Journal of Fluid Mechanics 538, 71–110. doi:10.1017/S0022112005005288.

Sørensen, J.N., Mikkelsen, R., Henningson, D.S., Ivanell, S., Sarmast, S., Andersen, S.J., 2015. Simulation of wind turbine wakes using the actuator line technique. Royal Society of London. Philosophical Transactions A. Mathematical, Physical and
480 Engineering Sciences 373, 20140071– 20140071. doi:10.1098/rsta.2014.0071.

Sørensen, J.N., Shen, W.Z., Munduate, X., 1998. Analysis of wake states by a full-field actuator disc model. Wind Energy 1, 73–88. doi: https://doi.org/10.1002/(SICI)1099-1824(199812)1:2<73::AID-WE12>3.0.CO;2-L.

Sørensen, N., 1995. General purpose flow solver applied to flow over hills. Ph.D. thesis. Risø National Laboratory. Published 2003.

485 Stankiewicz, W., Morzynski, M., Kotecki, K., Noack, B.R., 2017. On the need of mode interpolation for data-driven Galerkin models of a transient flow around a sphere. Theoretical and Computational Fluid Dynamics 31, 111–126. doi:10.1007/s00162-016-0408-7.

Taira, K., Brunton, S.L., Dawson, S.T., Rowley, C.W., Colonius, T., McKeon, B.J., Schmidt, O.T., Gordeyev, S., Theofilis, V., Ukeiley, L.S., 2017. Modal analysis of fluid flows: An overview. Aiaa Journal 55, 4013–4041. doi:10.2514/1.J056060.

490 Technical University of Denmark, 2022. Sophia hpc cluster. URL: https://dtu-sophia.github.io/docs/, doi:10.57940/FAFC-6M81.

Vermeer, N.J., Sørensen, J., Crespo, A., 2003. Wind turbine wake aerodynamics. Progress in Aerospace Sciences - PROG AEROSP SCI 39, 467– 510. doi:10.1016/S0376-0421(03)00078-2.

Xiao, D., Fang, F., Pain, C., Navon, I., 2017. A parameterized nonintrusive reduced order model and error analysis for general 495 timedependent nonlinear partial differential equations and its applications. Computer Methods in Applied Mechanics and Engineering 317, 868–889. doi:10.1016/j.cma.2016.12.033.